

Origin of efficient thermoelectric performance in half-Heusler FeNb_{0.8}Ti_{0.2}Sb

Hong-Jie Pang,¹ Chen-Guang Fu,² Hao Yu,¹ Liu-Cheng Chen,¹ Tie-Jun Zhu,² and Xiao-Jia Chen^{1,a)}

HPSTAR
592-2018

¹Center for High Pressure Science and Technology Advanced Research, Shanghai 201203, China

²State Key Laboratory of Silicon Materials, School of Materials Science and Engineering, Zhejiang University, Hangzhou 310027, China

(Received 27 March 2018; accepted 31 May 2018; published online 19 June 2018)

A half-Heusler material FeNb_{0.8}Ti_{0.2}Sb has been identified as a promising thermoelectric material due to its excellent thermoelectric performance at high temperatures. The origin of the efficient thermoelectric performance is investigated through a series of low-temperature (2–400 K) measurements. The high data coherence of the low and high temperatures is observed. An optimal and nearly temperature-independent carrier concentration is identified, which is ideal for the power factor. The obtained single type of hole carrier is also beneficial to the large Seebeck coefficient. The electronic thermal conductivity is found to be comparable to the lattice thermal conductivity and becomes the dominant component above 200 K. These findings again indicate that electron scattering plays a key role in the electrical and thermal transport properties. The dimensionless figure of merit is thus mainly governed by the electronic properties. These effects obtained at low temperatures with the avoidance of possible thermal fluctuations together offer the physical origin for the excellent thermoelectric performance in this material. *Published by AIP Publishing.*

<https://doi.org/10.1063/1.5030938>

I. INTRODUCTION

Thermoelectric materials have attracted a great deal of interest due to their remarkable applications in meeting the world's demand for generating electricity from waste heat and solid-state Peltier coolers.^{1–3} The thermoelectric efficiency of a material is determined by the dimensionless figure of merit,^{4,5} defined as $zT = S^2\sigma T/\kappa = PF T/\kappa$, where S is the Seebeck coefficient, σ is the electrical conductivity, T is the absolute temperature, κ is the total thermal conductivity (including the lattice contribution κ_l and the electron contribution κ_e), and PF is the power factor ($PF = S^2\sigma$). $zT = 3$ is needed for thermoelectric energy converters to compete with mechanical power generation and active refrigeration. However, state-of-the-art commercially available thermoelectric materials have a peak zT value less than unity. As a result, a material suitable for thermoelectric applications must be optimized through electrical conductivity, Seebeck coefficient, and thermal conductivity. However, aside from the independent parameter lattice thermal conductivity, the other transport properties (electrical conductivity, Seebeck coefficient, and electronic thermal conductivity) cannot be independently tuned in an effort to increase zT because the properties are interdependent via the carrier concentration (n) in a given thermoelectric material.^{3,6,7} Therefore, the main conventional efforts for maximizing the zT of thermoelectric materials are carrier concentration optimization^{3,8,9} and lattice thermal conductivity reduction.^{10–12} It is well known that the optimal carrier concentration depends on the temperature and band structure of thermoelectric semiconductors. Consequently, there are two major approaches used separately or in conjunction to achieve higher zT : One is to

find new crystalline materials with unique structural property relationships that yield the desired combination of properties,^{3,13–16} and the other is to utilize band engineering,^{17,18} alloying,¹⁹ or nanostructuring^{20,21} to tune the electrical and thermal transport properties.

Half-Heusler compounds with a valence electron count of 18 have recently been identified as promising thermoelectric materials due to their unique XYZ structures.^{22–24} These phases are well-known semiconductors with a narrow energy gap and sharp density of state slope near the Fermi level, which could potentially provide a higher Seebeck coefficient and moderate electrical conductivity.^{25–29} Nevertheless, the lattice thermal conductivity is relatively high.^{30–33} Among them, p -type FeNb_{0.8}Ti_{0.2}Sb is notably more competitive not only because its elements are inexpensive and Hf-free but it also possesses a relatively low lattice thermal conductivity. More importantly, FeNb_{0.8}Ti_{0.2}Sb exhibits excellent thermoelectric performance at high temperatures (> 900 K). The zT is superior to the optimized typical half-Heusler compounds,^{34–36} and its maximum zT (1.1 at 1100 K)³⁷ is almost twice as high as that of the most widely used p -type silicon-germanium thermoelectric materials.^{12,38–41} Fu *et al.*³⁷ also confirmed the good experimental repeatability and high-temperature stability of FeNb_{0.8}Ti_{0.2}Sb. Although the excellent high-temperature thermoelectric performance of FeNb_{0.8}Ti_{0.2}Sb is known, its physical mechanisms remain unclear.⁴² The study of a material's properties at low temperatures without thermal fluctuations is essential to have a real understanding of the physical origin of its good performance at high temperatures.

In this work, we present a series of low-temperature investigations of FeNb_{0.8}Ti_{0.2}Sb in order to obtain the physical origin of its excellent thermoelectric performance at high

^{a)}Electronic mail: xjchen@hpstar.ac.cn

temperatures. The physical mechanisms for low-temperature electrical and thermal properties are revealed. Moreover, the high data coherence of low and high temperatures is observed. Thus, the physical mechanisms at low temperatures are extended to high temperatures.

II. EXPERIMENTAL DETAILS

The sample ingot with a nominal composition of $\text{FeNb}_{0.8}\text{Ti}_{0.2}\text{Sb}$ used in the experiment was synthesized by levitation melting.³⁷ The obtained ingot was mechanically milled to obtain fine-grained powders. Afterwards, the powders were immediately impacted by spark plasma sintering at 1123 K for 10 min under 65 MPa in a vacuum; for a more detailed explanation, refer to Fu *et al.*³⁷ The as-sintered samples were annealed at 1123 K for 8 days. The phase structures of the sample were investigated by X-ray diffraction on a RigakuD/MAX-2550PC diffractometer using $\text{Cu-K}\alpha$ radiation ($\lambda_0 = 1.5406 \text{ \AA}$), and the chemical compositions were checked with an Energy Dispersive Spectrometer on an OXFORD X-Max^N. Magnetic susceptibility measurements were carried out in the temperature range of 1.8–300 K and in magnetic fields up to 5 T using a Magnetic Property Measurement System (Quantum Design). The electrical conductivity, Seebeck coefficient, and thermal conductivity measurements were performed from 2 K to 400 K using the thermal transport option (TTO) of a Physical Property Measurement System (Quantum Design). The Hall coefficient and specific heat measurements were also completed in the temperature range of 1.8–400 K using a Physical Property Measurement System (Quantum Design). For high-temperature (300–1100 K), the electrical conductivity and Seebeck coefficient were measured on a commercial Linseis LSR-3 system, and the thermal conductivity was estimated by a laser flash method on a Netzsch LFA457 instrument with a Pyroceram standard.

III. RESULTS AND DISCUSSION

A. Structural and composition characterization

The X-ray diffraction pattern of the sample, as shown in Fig. 1, was fully indexed within a cubic face-centered unit

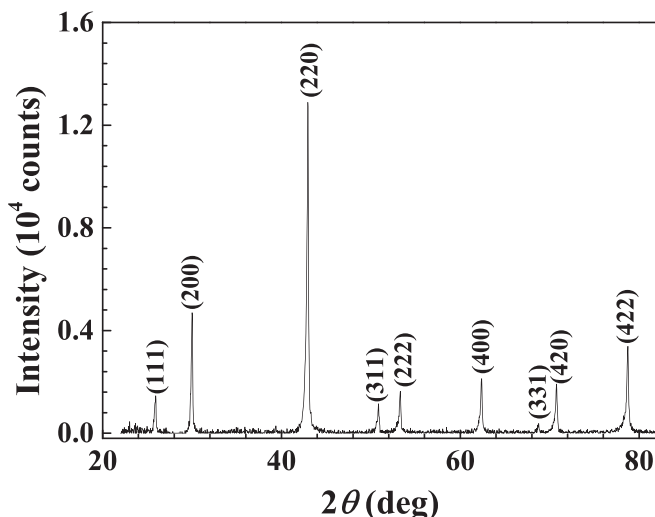


FIG. 1. X-ray diffraction pattern of $\text{FeNb}_{0.8}\text{Ti}_{0.2}\text{Sb}$.

cell with a lattice parameter of $a = 5.951 \text{ \AA}$. Compared with the database, the intensities of the diffraction peaks belong to a space group of $F\bar{4}3m$ which is consistent with the literature.⁴³ Table I shows the atomic distribution of the sample. The chemical composition of the sample determined using an Energy Dispersive Spectrometer was $\text{FeNb}_{0.8}\text{Ti}_{0.2}\text{Sb}$. The relative density of the sample is about 95%.

B. Magnetic characterization

Figure 2(a) shows the temperature dependencies of the zero-field-cooled (ZFC) and field-cooled (FC) magnetic susceptibility curves of $\text{FeNb}_{0.8}\text{Ti}_{0.2}\text{Sb}$ with the external field of 100 Oe together with the inverse magnetic susceptibility (χ^{-1}) data in the FC run between 1.8 K and 300 K. Both the ZFC and FC magnetic susceptibilities increase with decreasing temperature, exhibiting a sharp increase at lower temperatures below 6 K. A peak in ZFC is observed around 10 K, and irreversibility in ZFC and FC curves occurs below 200 K. A divergence in ZFC and FC along with a peak in the ZFC curves has been reported in the systems^{44–48} that possess mixed exchange interactions, such as spin glass and superparamagnetic or magnetic clusters. Taking other Heusler alloys for reference, the present results suggest that the sample is magnetically disordered. The broad maximum in the ZFC curve suggests the presence of distribution of magnetic clusters/defects.⁴⁴ On the other hand, superparamagnetism could also be taken into account.⁴⁴ With decreasing temperature, the inverse magnetic susceptibility follows a Curie-Weiss law above 135 K, indicating a paramagnetic behavior. However, it deviates markedly from the Curie-Weiss law below 135 K. The Curie-Weiss law has the following formula: $\chi(T) = \chi_0 + C/(T - T_C)$, where $C = N_A \mu_{\text{eff}}^2 / (3k_B)$, N_A is Avogadro's number, μ_{eff} is the effective moment, μ_B is the Bohr magneton, and T_C is the Curie-Weiss temperature. A least-squares fit of the inverse magnetic susceptibility from 135 K to 300 K is shown in Fig. 2. The excellent fitting indicates the onset of weak antiferromagnetism below 135 K. The antiferromagnetism is probably a result of atomic disorder.^{49–51}

In order to identify the magnetic phase at lower temperatures below 10 K, we investigate the magnetization (M) vs magnetic field (H) at 1.8 K shown in Fig. 2(b). Superparamagnetism is a form of magnetism which appears in small ferromagnetic or ferrimagnetic nanoparticles. In the absence of an external magnetic field, when the time used to measure the magnetization of the nanoparticles is much longer than the Néel relaxation time, their magnetization appears to be on average zero. However, ferromagnetism is a form of magnetism which could exhibit spontaneous magnetization: a net magnetic moment in the absence of an external magnetic field. As shown in Fig. 3, a so small amount of hysteresis exists at

TABLE I. Atomic distribution of $\text{FeNb}_{0.8}\text{Ti}_{0.2}\text{Sb}$.

Element	Ti	Fe	Nb	Sb
Atomic%	6.31	33.09	27.29	33.32

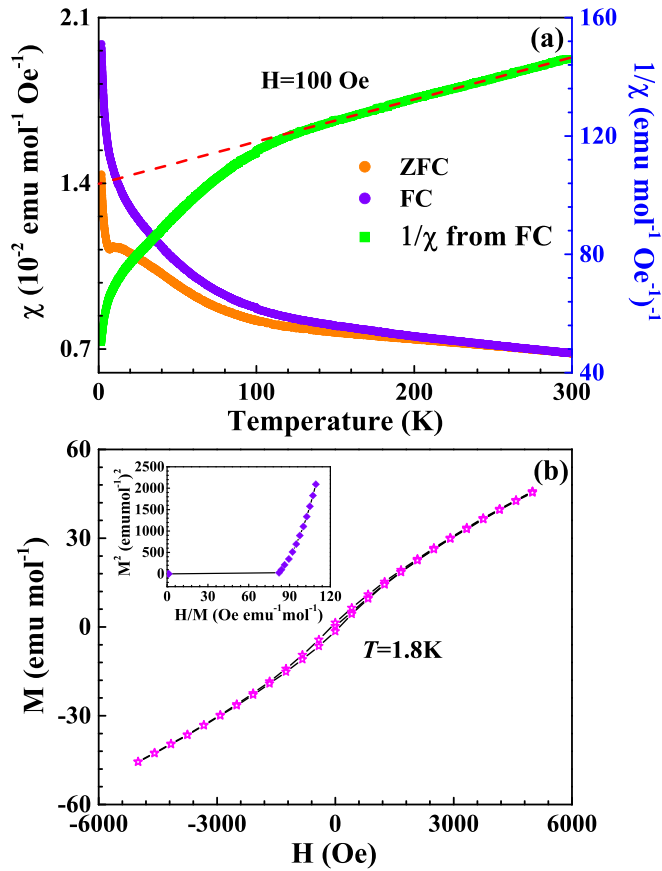


FIG. 2. (a) Magnetic susceptibility and the inverse susceptibility vs temperature for FeNb_{0.8}Ti_{0.2}Sb. The dotted line represents the linear extrapolation of the inverse susceptibility vs temperature plots. (b) Magnetization vs magnetic field at 1.8 K. Inset: Arrott plot at 1.8 K of FeNb_{0.8}Ti_{0.2}Sb.

1.8 K. This is a good indication of the presence of either superparamagnetism or weak ferromagnetism because a small hysteresis will also occur in superparamagnetism below the blocking temperature.^{44,52} Therefore, a further investigation of magnetic properties is needed. An Arrott

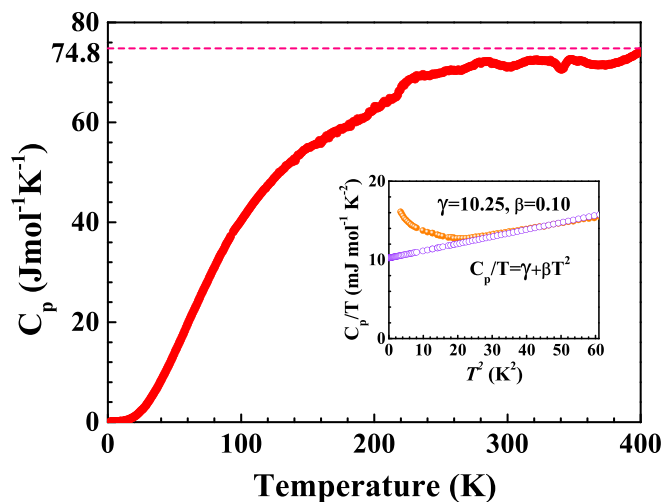


FIG. 3. Temperature dependence of specific heat of FeNb_{0.8}Ti_{0.2}Sb. The inset presents the low-temperature data as C_p/T vs T^2 function. The dotted line is the least-squares fit according to the equation above.

plot (M^2 vs H/M) of the $M(H)$ data for $H \leq 5$ kOe at 1.8 K is presented in the inset of Fig. 2(b). The Arrott plots are not linear, and the slope is positive, further confirming the superparamagnetism and ruling out the possibility of ferromagnetism.⁴⁴ The occurrence of hysteresis is due to freezing of the superparamagnetism below 10 K.⁴⁴ The presence of the antiferromagnetic state and superparamagnetic clusters below 135 K and 10 K, respectively, in the sample thus can be explained by the existence of atomic disorder. We must emphasize that the exact identification of Heusler alloys remains unsettled.^{44–52} The magnetic characterization of the sample is not the focus of this article. We concentrate more on the thermoelectric properties and their origin.

C. Specific heat

Figure 3 presents the temperature dependence of specific heat C_p of FeNb_{0.8}Ti_{0.2}Sb. The specific heat curve has a typical sigmoid like shape and approaches a value expected from the Dulong-Petit law, $C_p = 3NR = 74.8 \text{ J mol}^{-1} \text{ K}^{-1}$, where N is the number of atoms per molecule and R is the gas constant. At very low temperatures, the specific heat in FeNb_{0.8}Ti_{0.2}Sb gradually diminishes to zero. The inset in Fig. 3 shows the low temperature dependence of specific heat presented as C_p/T vs T^2 from 5 K to 10 K. It can be well described by the formula⁵³

$$C_p = \gamma T + \beta T^3,$$

where γT and βT^3 are the electron and phonon contributions to the total specific heat, respectively. As a result, the coefficient γ is $10.25 \text{ mJ mol}^{-1} \text{ K}^{-2}$, and β is $0.10 \text{ mJ mol}^{-1} \text{ K}^{-4}$. From the value of β , one can estimate the Debye temperature $\Theta_D = (12R\pi^4 n/5\beta)^{1/3}$ to be about 388 K. The abnormal upturn seen at low temperature is similar to that observed in several systems, including the new iron-based superconductors and other Heusler materials.^{54–56} For FeNb_{0.8}Ti_{0.2}Sb, the phenomenon may originate from the magnetic clusters arising from the atomic disorder.

It is noteworthy that a theoretical estimation of the thermal conductivity using the Debye theory could reveal a relationship between the thermal conductivity and specific heat, which is given by $\kappa = \frac{1}{3} C \nu l$, where C is the specific heat per volume, ν is the average phonon velocity, and l is the phonon mean free path. At very low temperatures, the low specific heat indicates low thermal conductivity. With increasing temperature, the specific heat increases quickly and approaches a constant value. Therefore, the thermal conductivity increases rapidly and also reaches a maximum. At higher temperatures, with the enhancement of the phonon-phonon scattering, the average phonon velocity and phonon mean free path are limited significantly and the thermal conductivity greatly reduces.

D. Electrical transport properties

Figure 4 illustrates the temperature dependencies of (a) electrical conductivity and (b) Seebeck coefficient of FeNb_{0.8}Ti_{0.2}Sb. The high-temperature data taken from the LSR-3 system are shown in red for comparison. As figures

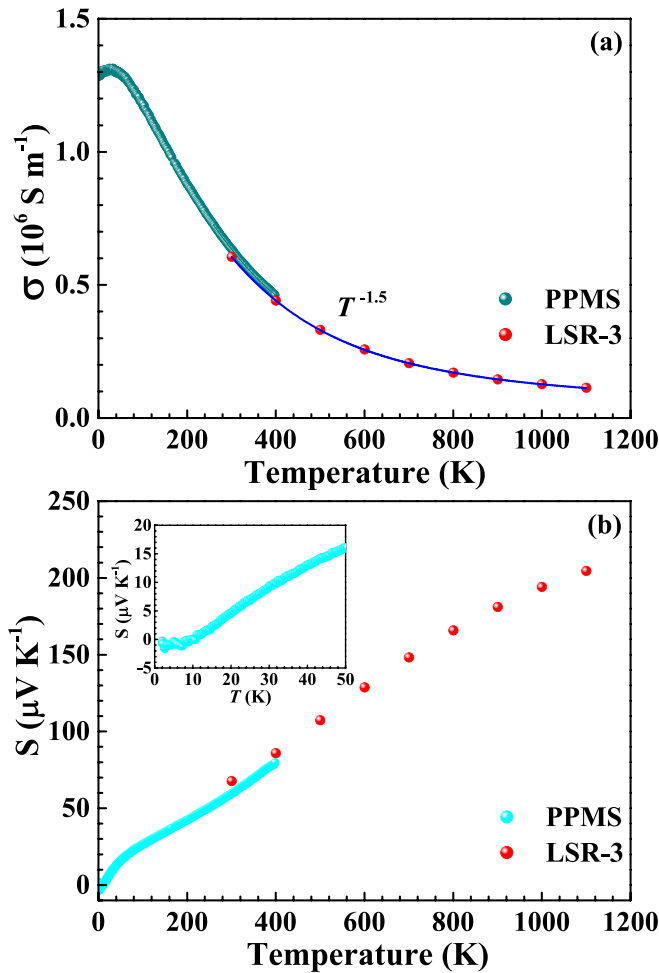


FIG. 4. Temperature dependencies of (a) the electrical conductivity and (b) Seebeck coefficient of $\text{FeNb}_{0.8}\text{Ti}_{0.2}\text{Sb}$. The inset of (b) shows the temperature dependence of the Seebeck coefficient below 50 K. The high-temperature data taken from a LSR-3 system are shown in red for comparison.

show, the low and high temperature electrical transport properties measured by different methods are consistent with each other. In addition, the low and high temperature data converge at room temperature. As temperature is increased, the electrical conductivity decreases rapidly in the range of 10^6 S m^{-1} , following degenerate semiconducting behavior.⁵⁷ This implies that the electrical conductivity will follow a temperature dependence of $T^{-1.5}$ from the Debye temperature (388 K) to the intrinsic excitation temperature,⁵⁸ which agrees well with the high-temperature experimental data (388 K–1100 K). Therefore, acoustic phonon scattering dominates charge transport,⁵⁹ which is consistent with the specific heat measurement, where there is an upturn at low temperatures (below 30 K). The anomalous temperature dependence of electrical conductivity maybe due to the magnetic clusters arising from the atomic disorder.⁵⁶

The values of the Seebeck coefficient are negative below 10 K and remain positive from 10 K to 1100 K. As temperature is increased, the Seebeck coefficient increases rapidly and approaches $80 \mu\text{V K}^{-1}$ in the vicinity of 400 K and a maximum of $205 \mu\text{V K}^{-1}$ at 1100 K, which is a typical behavior for degenerate semiconductors.⁵⁷ Thus, it can be predicted that the Seebeck coefficient will

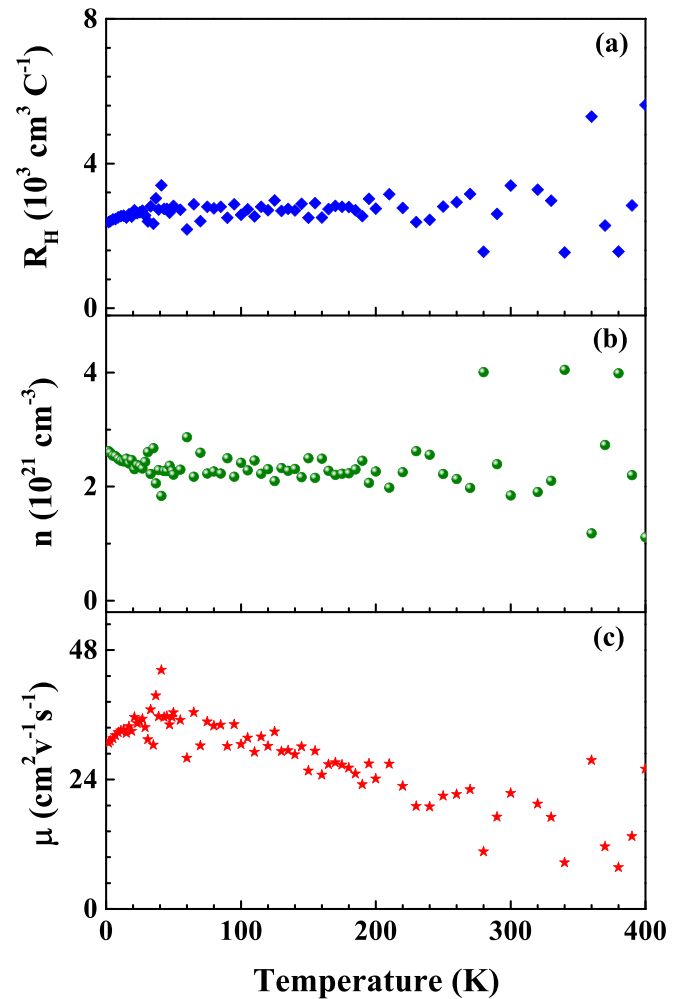


FIG. 5. Temperature dependencies of (a) the Hall coefficient, (b) carrier concentration, and (c) carrier mobility of $\text{FeNb}_{0.8}\text{Ti}_{0.2}\text{Sb}$.

linearly increase with increasing temperature before the intrinsic excitation which is in accordance with the high-temperature data.

For $\text{FeNb}_{0.8}\text{Ti}_{0.2}\text{Sb}$, the carrier concentration is one of the most important physical parameters for thermoelectric performance. The electrical conductivity is related to the carrier concentration through the carrier mobility (μ): $\sigma = ne\mu$, where e is the unit charge. The carrier concentration is calculated by $n = 1/eR_H$, where R_H is the Hall coefficient.³⁷ Figure 5 shows the temperature dependencies of (a) the Hall coefficient, (b) the calculated carrier concentration, and (c) the carrier mobility of $\text{FeNb}_{0.8}\text{Ti}_{0.2}\text{Sb}$ from 1.8 K to 400 K, respectively. The carrier concentration is rather constant and almost independent of temperature, about 10^{21} cm^{-3} below 400 K which is in the optimal theoretical value range.^{3,37} The carrier mobility decreases slightly with temperature and becomes $25 \text{ cm}^2 \text{ v}^{-1} \text{ s}^{-1}$ at 400 K, which is consistent with the electrical conductivity. The Hall coefficient values are positive and remain stable over the whole low temperature range, indicating that the majority of the charge carriers are holes and there is only a single type of carrier that will benefit the Seebeck coefficient. For degenerate semiconductors, the Seebeck coefficient is given by²¹

$$S = \frac{8\pi^2 \kappa_B^2 T}{3eh^2} m^* \left(\frac{\pi}{3n} \right)^{2/3},$$

where m^* is the effective mass of the carrier. Thus, the large Seebeck coefficient is due to the optimal carrier concentration and hole carriers, which have a larger effective mass than the electrons. The effective mass was calculated using a single parabolic band (SPB) model. The band effective mass value is $1.6m_e$.³⁷ Below 10 K, the values of the Seebeck coefficient are below zero, implying that the effective mass is negative. This means that the band curves downwards away from a maximum. Taking into account the magnetic properties of FeNb_{0.8}Ti_{0.2}Sb, the magnetic clusters arising from the atomic disorder in the sample may contribute to the phenomenon.

E. Thermal transport properties

Figure 6 presents the temperature dependence of the thermal conductivity of FeNb_{0.8}Ti_{0.2}Sb and high-temperature data estimated by a laser flash method on a Netzsch LFA457 instrument with a Pyroceram standard. The low-temperature data agree well with the high-temperature data measured using different methods. As temperature is increased, the thermal conductivity increases rapidly and reaches a maximum (approximately 8.7 WK⁻¹ m⁻¹) around 126 K and then declines gradually, which is in accordance with the specific heat estimation.

The inset shows the temperature dependencies of the lattice and electron components of the thermal conductivity of FeNb_{0.8}Ti_{0.2}Sb. The lattice thermal conductivity was obtained by subtracting the electron component from the total thermal conductivity. The electronic thermal conductivity was calculated via $\kappa_e = L\sigma T = Lne\mu T$, where L is the Lorenz number and can be calculated using the SPB model with reasonable approximation.⁶⁰ The temperature dependence of the lattice thermal conductivity is similar to that of

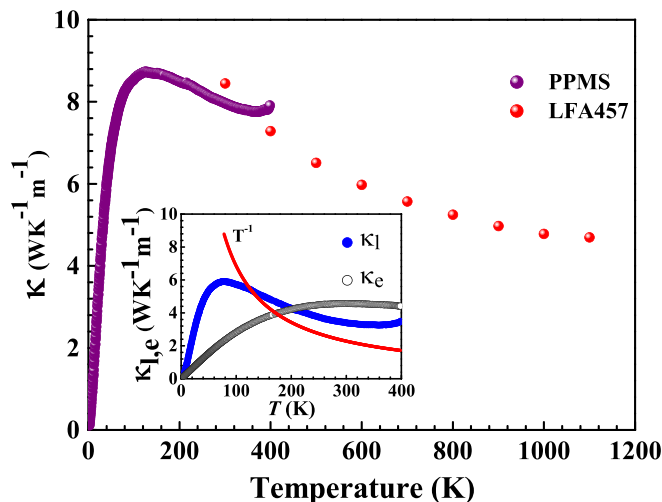


FIG. 6. Temperature dependence of the thermal conductivity of FeNb_{0.8}Ti_{0.2}Sb and high-temperature data (in red) estimated by a laser flash method on a Netzsch LFA457 instrument with a Pyroceram standard. The inset shows the temperature dependence of the lattice and electron components of the thermal conductivity of FeNb_{0.8}Ti_{0.2}Sb.

the total thermal conductivity. The maximum is 5.9 WK⁻¹ m⁻¹ around 77 K, which is relatively low compared to the sample with a lower Ti content.³⁷

The scattering mechanism could further explain the shape of the observed lattice thermal conductivity curve as follows: the lattice thermal conductivity is typically limited by normal three-phonon scattering, umklapp scattering, impurity scattering, and boundary scattering.⁶¹ At very low temperatures, boundary scattering dominates the scattering mechanism, and the lattice thermal conductivity is small. As temperature is increased, the impurity scattering becomes important because it becomes easier to create higher frequency phonons that are scattered efficiently by point impurities. Therefore, the lattice thermal conductivity reaches a maximum and then declines. As temperature is increased further, normal three-phonon scattering and umklapp scattering gradually come to dominate. At higher temperatures, all phonon scattering occupies the scattering mechanism.

Disorder in the crystal lattice would increase phonon scattering and reduce the lattice thermal conductivity due to point defect scattering and also exhibit a possible broad Umklapp peak. We fitted the temperature dependence of the lattice thermal conductivity above the temperature of the Umklapp peak. As can be seen in the inset of Fig. 6, the experimental data obviously exhibit a lower decay rate of T^{-1} . It can be expected from the influence of strong point defect scattering.⁶² In previous work, the carrier mean path in the p -type FeNbSb was comparable to the lattice parameter, indicating that the carrier mobility of this system almost reaches the Ioffe-Regel limit,⁶³ which means that the carrier scattering has reached the highest limit and introducing more phonon scattering centers will not impair the power factor but largely suppress the lattice thermal conductivity.⁵⁷ For semiconductors, the electronic thermal conductivity is much less than the lattice thermal conductivity, whereas the electron contribution to the total thermal conductivity of FeNb_{0.8}Ti_{0.2}Sb is significant. As shown in Fig. 6, the electronic thermal conductivity increases with temperature and becomes higher than the lattice thermal conductivity from 200 K.

To minimize the lattice thermal conductivity, disorder within the unit cell,¹⁰ superlattices,⁶⁴ complex unit cells,⁶⁵ and nanostructures⁶⁶ have been widely used in thermoelectric materials over the past few years. For FeNb_{0.8}Ti_{0.2}Sb, the electronic thermal conductivity is comparable to or even higher than the lattice thermal conductivity above 200 K. This means that the lattice thermal conductivity is largely suppressed and the thermal conductivity is mainly determined by the electronic thermal conductivity.

F. Figure of merit zT

Figure 7 shows the temperature dependence of zT of FeNb_{0.8}Ti_{0.2}Sb in the temperature range of 1.8–400 K, together with the high-temperature data measured by a different method for comparison. As the intensive result of the electrical conductivity, Seebeck coefficient, and thermal conductivity, the zT exhibits a pronounced rise with temperature. Thereafter, it continuously increases to 0.14 around 400 K

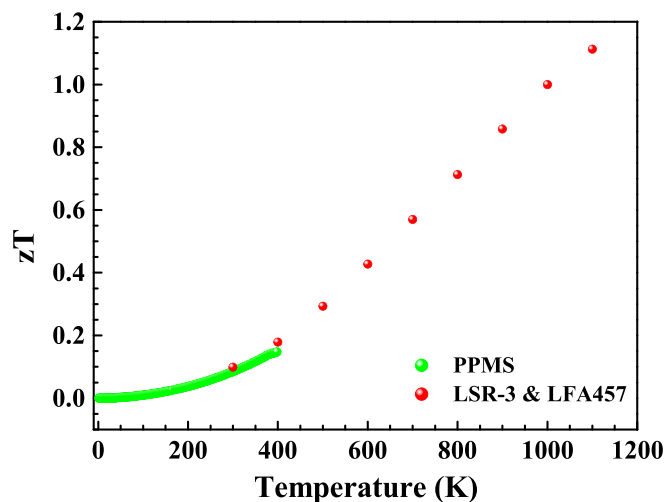


FIG. 7. Temperature dependence of zT of $\text{FeNb}_{0.8}\text{Ti}_{0.2}\text{Sb}$. The data at high temperatures (in red) are taken from a LSR-3 system and a Netzsch LFA457 instrument.

and reaches a maximum of 1.1 at 1100 K. Compared with other high temperature thermoelectric materials, $\text{FeNb}_{0.8}\text{Ti}_{0.2}\text{Sb}$ exhibits excellent thermoelectric performance for power generation, and its zT exceeds the industry benchmarks set by p -type silicon-germanium high-temperature alloys.⁶⁷ Furthermore, it is better than the optimized n -type (Hf, Zr)NiSn half-Heusler compound (the maximum zT is 1.0 at 1000 K).^{34–36} The low temperature and high temperature values of zT connect well and converge around room temperature. The trend demonstrated in the case of low temperature is extended to high temperature. This means that the large Seebeck coefficient, the moderate electrical conductivity, and the relatively low thermal conductivity at low temperatures, which result from an optimal and temperature-independent carrier concentration and a high content of Ti doping, will continue to contribute to the thermoelectric performance at high temperatures. The thermoelectric power factor is essentially determined by electronic properties and so is the thermal conductivity. Based on the above consideration, the zT of $\text{FeNb}_{0.8}\text{Ti}_{0.2}\text{Sb}$ is mainly governed by its electronic properties.

IV. CONCLUSIONS

In conclusion, we have performed electrical and thermal transport measurements on $\text{FeNb}_{0.8}\text{Ti}_{0.2}\text{Sb}$ at low temperatures in order to elucidate the physical origin of the high thermoelectric performance, avoiding the influence of thermal fluctuations. The low-temperature trend of the electrical conductivity, Seebeck coefficient, and thermal conductivity is extended to high temperature. The optimized power factor mostly results from the optimal and almost temperature-independent carrier concentration. Meanwhile, a single type of hole carrier benefits the Seebeck coefficient as well. The lattice thermal conductivity is largely suppressed, and the total thermal conductivity is mainly determined by the electronic thermal conductivity. Consequently, the zT of $\text{FeNb}_{0.8}\text{Ti}_{0.2}\text{Sb}$ is mainly governed by its electronic

properties. As a result, the zT exhibits a pronounced rise from the low to high temperatures and approaches a maximum of 1.1 at 1100 K, exceeding state-of-the-art thermoelectric materials. These findings highlight that investigating the low-temperature physical properties of thermoelectric materials can help to obtain thorough knowledge of their behavior at high temperatures.

ACKNOWLEDGMENTS

We thank Yanping Yang for her help in the Energy Dispersive Spectrometer measurement. The sample preparation was supported by the Natural Science Foundation of China (No. 11574267).

- ¹F. J. DiSalvo, *Science* **285**, 703 (1999).
- ²G. S. Nolas, D. T. Monelli, and T. M. Tritt, *Annu. Rev. Mater. Sci.* **29**, 89 (1999).
- ³G. J. Snyder and E. S. Toberer, *Nat. Mater.* **7**, 105 (2008).
- ⁴T. M. Tritt, *Science* **283**, 804 (1999).
- ⁵G. D. Mahan and J. O. Sofo, *Proc. Natl. Acad. Sci. U.S.A.* **93**, 7436 (1996).
- ⁶G. S. Nolas, J. L. Cohn, and G. A. Slack, *Phys. Rev. B* **58**, 164 (1998).
- ⁷G. S. Nolas, T. J. R. Weakley, and J. L. Cohn, *Chem. Mater.* **11**, 2470 (1999).
- ⁸H. Yu, L. C. Chen, H. J. Pang, X. Y. Qin, P. F. Qiu, X. Shi, L. D. Chen, and X. J. Chen, *Chem. Mater. Today Phys.* **5**, 1 (2018).
- ⁹L. C. Chen, H. Yu, H. J. Pang, B. B. Jiang, L. Su, X. Shi, L. D. Chen, and X. J. Chen, "Pressure-induced enhancement of thermoelectric performance in palladium sulfide," *Mater. Today Phys.* (in press).
- ¹⁰B. C. Sales, D. Mandrus, and R. K. Williams, *Science* **272**, 1325 (1996).
- ¹¹K. F. Hsu, S. Loo, F. Guo, W. Chen, J. S. Dyck, C. Uher, T. Hogan, E. K. Polychroniadis, and M. G. Kanatzidis, *Science* **303**, 818 (2004).
- ¹²B. Poudel, Q. Hao, Y. Ma, Y. C. Lan, A. Minnich, B. Yu, X. A. Yan, D. Z. Wang, A. Muto, D. Vashaee, X. Y. Chen, J. M. Liu, M. S. Dresselhaus, G. Chen, and Z. F. Ren, *Science* **320**, 634 (2008).
- ¹³T. M. Tritt and M. A. Subramanian, *MRS Bull.* **31**, 188 (2006).
- ¹⁴C. Yu, T. J. Zhu, R. Z. Shi, Y. Zhang, X. B. Zhao, and J. He, *Acta Mater.* **57**, 2757 (2009).
- ¹⁵S. M. Kauzlarich, S. R. Brown, and G. J. Snyder, *Dalton Trans.* **21**, 2099 (2007).
- ¹⁶S. R. Brown, S. M. Kauzlarich, F. Gascoin, and G. J. Snyder, *Chem. Mater.* **18**, 1873 (2006).
- ¹⁷J. P. Heremans, V. Jovic, E. S. Toberer, A. Saramat, K. Kurosaki, A. Charoenphakdee, S. Yamanaka, and G. J. Snyder, *Science* **321**, 554 (2008).
- ¹⁸J. P. Heremans, B. Wiendlocha, and A. M. Chamoine, *Energy Environ. Sci.* **5**, 5510 (2012).
- ¹⁹K. Biswas, J. He, I. D. Blum, C. I. Wu, T. P. Hogan, D. N. Seidman, V. P. Draid, and M. G. Kanatzidis, *Nature* **489**, 414 (2012).
- ²⁰J. Yang, G. P. Meisner, and L. D. Chen, *Appl. Phys. Lett.* **85**, 1140 (2004).
- ²¹S. Sakurada and N. Shutoh, *Appl. Phys. Lett.* **86**, 082105 (2005).
- ²²C. G. Fu, S. Q. Bai, Y. T. Liu, Y. S. Tang, L. D. Chen, X. B. Zhao, and T. J. Zhu, *Nat. Commun.* **6**, 8144 (2015).
- ²³T. J. Zhu, C. G. Fu, H. H. Xie, Y. T. Liu, and X. B. Zhao, *Adv. Energy Mater.* **5**, 1500588 (2015).
- ²⁴S. Chen and Z. F. Ren, *Mater. Today* **16**, 387 (2013).
- ²⁵F. G. Aliev, V. V. Kozyrkov, V. V. Moshchalkov, R. V. Scolozdra, and K. Durczewski, *Z. Phys. B: Condens. Matter* **80**, 353 (1990).
- ²⁶I. Galanakis, P. H. Dederichs, and N. Papanikolaou, *Phys. Rev. B* **66**, 134428 (2002).
- ²⁷J. Yang, H. Li, T. Wu, W. Q. Zhang, L. Q. Chen, and J. H. Yang, *Adv. Funct. Mater.* **18**, 2880 (2008).
- ²⁸J. W. Simonson and S. J. Poon, *J. Phys.: Condens. Matter* **20**, 255220 (2008).
- ²⁹G. Joshi, R. He, M. Engber, G. Samsonidze, T. Pantha, E. Dahal, K. Dahal, J. Yang, Y. C. Lan, B. Kozinsky, and Z. F. Ren, *Energy Environ. Sci.* **7**, 4070 (2014).
- ³⁰H. Honl, A. P. Ramirez, C. Goldmann, G. Ernst, B. Wölfing, and E. Bucher, *J. Phys.: Condens. Matter* **11**, 1697 (1999).

- ³¹C. Uher, J. Yang, S. Hu, D. T. Morelli, and G. P. Meisner, *Phys. Rev. B* **59**, 8615 (1999).
- ³²Y. Xia, S. Bhattacharya, V. Ponnambalam, A. L. Pope, S. J. Poon, and T. M. Tritt, *J. Appl. Phys.* **88**, 1952 (2000).
- ³³T. Sekimto, K. Kurosaki, H. Muta, and S. Yamanaka, *Mater. Trans.* **47**, 1445 (2006).
- ³⁴T. J. Zhu, K. Xiao, C. Yu, J. J. Shen, S. H. Yang, A. J. Zhou, and J. He, *J. Appl. Phys.* **108**, 044903 (2010).
- ³⁵R. A. Downie, S. R. Popuri, H. Ning, M. J. Reece, and J.-W. G. Bos, *Materials* **7**, 7093 (2014).
- ³⁶S. Chen, K. C. Lukas, W. Liu, C. P. Opeil, G. Chen, and Z. F. Ren, *Adv. Energy Mater.* **3**, 1210 (2013).
- ³⁷C. G. Fu, T. J. Zhu, Y. T. Liu, H. H. Xie, and X. B. Zhao, *Energy Environ. Sci.* **8**, 216 (2015).
- ³⁸M. Zebarjadi, G. Joshi, G. H. Zhu, B. Yu, A. Minnich, Y. C. Lan, X. W. Wang, M. Dresselhaus, Z. F. Ren, and G. Chen, *Nano Lett.* **11**, 2225 (2011).
- ³⁹B. Yu, M. Zebarjadi, H. Wang, K. Lukas, H. Z. Wang, D. Wang, C. Opeil, M. Dresselhaus, G. Chen, and Z. F. Ren, *Nano Lett.* **12**, 2077 (2012).
- ⁴⁰G. Joshi, X. Yan, H. Wang, W. Liu, G. Chen, and F. R. Ren, *Adv. Energy Mater.* **1**, 643 (2011).
- ⁴¹S. J. Poon, D. Wu, S. Zhu, W. J. Xie, T. M. Tritt, P. Thomas, and R. Venkatasubramanian, *J. Mater. Res.* **26**, 2795 (2011).
- ⁴²R. He, D. Kraemer, J. Mao, L. P. Zeng, Q. Jie, Y. C. Lan, C. H. Li, J. Shuai, H. S. Kim, Y. Liu, D. Broido, C. W. Chu, G. Chen, and Z. F. Ren, *Proc. Natl. Acad. Sci. U.S.A.* **113**, 13576 (2016).
- ⁴³F. Casper, T. Graf, S. Chadov, B. Balke, and C. Felser, *Semicond. Sci. Technol.* **27**, 063001 (2012).
- ⁴⁴M. Vasundhara, V. Srinivas, and V. V. Rao, *Phys. Rev. B* **78**, 064401 (2008).
- ⁴⁵A. E. Berkowitz, J. R. Mitchell, M. J. Carey, A. P. Young, S. Zhang, F. E. Spada, F. T. Parker, A. Hutten, and G. Thomas, *Phys. Rev. Lett.* **68**, 3745 (1992).
- ⁴⁶P. Allia, M. Knobel, P. Tiberto, and F. Vinai, *Phys. Rev. B* **52**, 15398 (1995).
- ⁴⁷M. Rubinstein, V. G. Harris, B. N. Das, and N. C. Koon, *Phys. Rev. B* **50**, 12550 (1994).
- ⁴⁸P. Allia, M. Coission, J. Moya, V. Selvaggini, P. Tiberto, and F. Vinai, *Phys. Rev. B* **67**, 174412 (2003).
- ⁴⁹A. Ślebarki, M. B. Maple, E. J. Freeman, C. Sirvent, D. Tworuszka, M. Orzechowska, A. Wrona, A. Jezierski, S. Chiuzbaian, and M. Neumann, *Phys. Rev. B* **62**, 3296 (2000).
- ⁵⁰C. S. Lue, Y. Li, J. H. Ross, Jr., and G. M. Irwin, *Phys. Rev. B* **67**, 224425 (2003).
- ⁵¹A. Ślebarki, J. Deniszczyk, W. Borgiel, A. Jezierski, M. Swatek, A. Winiarska, M. B. Maple, and W. M. Yuhasz, *Phys. Rev. B* **69**, 155118 (2004).
- ⁵²Y. Feng, J. Y. Rhee, T. A. Wiener, D. W. Lynch, B. E. Hubbard, A. J. Sievers, D. L. Schlagel, T. A. Lograsso, and L. L. Miller, *Phys. Rev. B* **63**, 165109 (2001).
- ⁵³K. Gofryk, D. Kaczorowski, T. Plackowski, J. Mucha, A. Leithe-Jasper, W. Schnelle, and Yu. Grin, *Phys. Rev. B* **75**, 224426 (2007).
- ⁵⁴J. S. Kim, E. G. Kim, and G. R. Stewart, *J. Phys.: Condens. Matter* **21**, 252201 (2009).
- ⁵⁵K. Gofryk, M. Pan, C. Cantoni, B. Saparov, J. E. Mitchell, and A. S. Sefat, *Phys. Rev. Lett.* **112**, 047005 (2014).
- ⁵⁶S. V. Dordevic, D. N. Basov, A. Ślebarki, M. B. Maple, and L. Degiorgi, *Phys. Rev. B* **66**, 075122 (2002).
- ⁵⁷C. G. Fu, H. J. Wu, Y. T. Liu, J. Q. He, X. B. Zhao, and T. J. Zhu, *Adv. Sci.* **3**, 1600035 (2016).
- ⁵⁸C. G. Fu, T. J. Zhu, Y. Z. Pei, H. H. Xie, H. Wang, G. J. Snyder, Y. Liu, Y. T. Liu, and X. B. Zhao, *Adv. Energy Mater.* **4**, 1400600 (2014).
- ⁵⁹X. Shi, Y. Z. Pei, G. J. Snyder, and L. D. Chen, *Energy Environ. Sci.* **4**, 4086 (2011).
- ⁶⁰H. H. Xie, H. Wang, Y. Z. Pei, C. G. Fu, X. H. Liu, G. J. Snyder, X. B. Zhao, and T. J. Zhu, *Adv. Funct. Mater.* **23**, 5123 (2013).
- ⁶¹J. Callaway, *Phys. Rev.* **113**, 1046 (1959).
- ⁶²H. H. Xie, H. Wang, C. G. Fu, Y. T. Liu, G. J. Snyder, X. B. Zhao, and T. J. Zhu, *Sci. Rep.* **4**, 6888 (2014).
- ⁶³M. Gurvitch, *Phys. Rev. B* **24**, 7404 (1981).
- ⁶⁴R. Venkatasubramanian, E. Siivola, T. Colpitts, and B. O'Quinn, *Nature (London)* **413**, 597 (2001).
- ⁶⁵D. Y. Chung, T. P. Hogan, M. Rocci-Lane, P. Brazis, J. R. Ireland, C. R. Kannewurf, M. Bastea, C. Uher, and M. G. Kanatzidis, *J. Am. Chem. Soc.* **126**, 6414 (2004).
- ⁶⁶T. J. Zhu, Y. Q. Cao, Q. Zhang, and X. B. Zhao, *J. Electron. Mater.* **39**, 1990 (2010).
- ⁶⁷A. Usenko, D. Moskovskikh, M. Gorshenkov, A. Voronin, A. Stepashkin, S. Kaloshkin, D. Arkhipov, and V. Khovaylo, *Scr. Mater.* **127**, 63 (2017).